Noncontinuum drag force on a nanowire vibrating normal to a wall: Simulations and theory

Shriram Ramanathan,[1] Donald L. Koch,[1] and Rustom B. Bhiladvala[2]
[1]*School of Chemical and Biomolecular Engineering, Cornell University, Ithaca, New York 14853-5201, USA*
[2]*Department of Mechanical Engineering, University of Victoria, Victoria, British Columbia V8W 3P6, Canada*

(Received 5 April 2010; accepted 25 August 2010; published online 21 October 2010)

Nanoelectromechanical oscillators are very attractive as sensing devices because of their low power requirements and high resolution, especially at low pressures. While many experimental studies of such systems are available in the literature, a fundamental theoretical understanding over the entire range of operating conditions is lacking. In this article, we use our newly developed Bhatnagar–Gross–Krook based low Mach number direct simulation Monte Carlo method to study the noncontinuum drag force acting on a cylinder oscillating normal to a wall. We explore quasisteady flows in which $\omega\tau_f \ll 1$ as well as unsteady flows for which $\omega\tau_f = O(1)$. Here ω is the oscillation frequency and τ_f is the characteristic time for the development of the gas flow. The drag force per unit length acting on a long cylindrical wire is studied as a function of the Knudsen number, defined in terms of the mean free path λ and the radius of the cylinder R as $\mathrm{Kn} = \lambda/R$. For quasisteady flows, we also present theoretical calculations for the slip regime, $\mathrm{Kn} \ll 1$, and the free molecular flow regime, $\mathrm{Kn} \gg 1$. Simulations of unsteady gas flow around a sinusoidally oscillating cylinder near a wall indicate that the drag force per unit length nondimensionalized by $4\pi\mu U$ approaches constant values for $\omega\tau_f \ll 1$ (quasisteady flow) and for $\omega\tau_f \gg 1$. Here μ is the gas viscosity and U is the maximum value of the nanowire velocity. The simulation results are compared with experimental measurements in the quasisteady regime. © *2010 American Institute of Physics*.
[doi:10.1063/1.3491127]

I. INTRODUCTION

Mechanically resonant microscale structures such as deflecting cantilevers and beams[1–3] have long been studied for use as sensing devices. Recently, there has been a considerable interest in sensors based on resonating nanoelectromechanical systems.[4–8] These nanoscale resonators show high resonant frequencies of the order of several megahertz and quality factors in the range 10^3–10^5 thus offering advantages over their micro- and macroscale counterparts such as lower energy dissipation, faster response times, and ultrahigh sensitivity.[5,9] Indeed, over the last few years, nanoscale oscillators have already been applied for fast detection of chemical[10] and biological entities[11] in small quantities, sensing of femtogram masses[12] and attonewton forces, and measurement of material properties.[13] All of these applications require a thorough understanding of the behavior of nanoscale resonators, which depends on the dissipation occurring in the solid and gas phases. In this article we attempt to understand the effects of noncontinuum and unsteady gas flows on the dissipation due to the gas.

Resonance based sensors operate by measuring changes in resonance frequency on attaching masses or applying forces. The resolution of the sensor depends on the sharpness of the resonance peak which is quantified by the quality factor defined as

$$\frac{1}{Q} = \frac{\mathrm{E_{diss}}}{2\pi \mathrm{E_{stored}}}, \tag{1}$$

where $\mathrm{E_{stored}}$ is the energy stored in the oscillating wire and $\mathrm{E_{diss}}$ is the energy dissipated per cycle. Energy dissipation occurs in the solid phase as well as the fluid phase. The solid dissipation can be attributed either to losses in the clamps supporting the resonator or to internal friction within the resonator and is the dissipation measured when the resonator operates in perfect vacuum. The fluid dissipation is attributable to frictional forces exerted by the surrounding gas on the resonator and exists only at nonzero gas pressures. For small nanowire deflections and velocities, the dissipation in the solid and fluid phases can be assumed to be decoupled and the total dissipation can be expressed as a linear superposition,

$$\mathrm{E_{diss}} = \mathrm{E^s_{diss}} + \mathrm{E^f_{diss}}, \tag{2}$$

of a solid dissipation $\mathrm{E^s_{diss}}$ and a fluid dissipation $\mathrm{E^f_{diss}}$.

Experimental studies[5–7,14,15] are in general agreement that the quality factor increases with decreasing gas pressure, reaching an asymptote determined solely by solid dissipation in a vacuum. However, there is little agreement among the studies on the dissipation in the presence of a gas and the experiments do not agree with the limited theoretical work that is currently available. A parametric study of the relevant

fluid dynamic problem may provide a framework in which to understand experimental results and inspire careful experimental measurements that characterize all the relevant parameters.

The resonators consist of long wires or beams with length L clamped at either one end or both ends. Experiments have been performed on beams with rectangular cross-sections and wires with circular cross-section. For simplicity, we will consider a circular cross-section of radius R. The wire is oscillating normal to a planar wall with a distance from the bottom of the wire to the wall of H. Most of the studies involve large aspect ratios $L/(2R) \geq 10$. Although the proximity of the bottom wall will have a large effect on the fluid dissipation, most experimental studies do not report values of H. Li *et al.*[7] report $H/R=1.8182$ and we will use this value in our simulation studies. It is reasonable to assume that H/R would be of order one in most experimental studies as this choice would be convenient in terms of the fabrication processes. When $L/(2R) \gg 1$ and $L/H \gg 1$, the gas flow can be considered a quasi-two-dimensional flow at any point along its length. We will make use of this important simplifying assumption in the simulations and analysis presented here.

Because of the small dimensions of the nanowires and the fact that experiments are sometimes performed at reduced pressure, the gas flow is typically in the transition flow regime. The Knudsen number, defined as $\mathrm{Kn}=\lambda/R$ where $\lambda=k_B T/(\sqrt{2}\pi p\sigma^2)$ is the mean free path varies in the experimental studies cited above from 10^{-3} to 10^{9}. We will present direct simulation Monte Carlo (DSMC) simulations for Knudsen numbers of the order of one along with slip flow theory for $\mathrm{Kn} \ll 1$ and free molecular flow theory for $\mathrm{Kn} \gg 1$. Here σ is the diameter of the molecule.

For a nanowire oscillating at a frequency ω, the instantaneous local displacement can be written as $y(z,t)=A(z)\cos(\omega t)$ where y represents the local position along the length of the nanowire and $A(z)$ is the local amplitude. The importance of nonlinear gas flow effects is measured by the Mach number $M=A\omega/\langle c\rangle$, where $\langle c\rangle=\sqrt{(8k_B T/\pi m)}$ is the mean molecular speed and m is the mass of a gas molecule. The experimental studies (with the exception of Ref. 14) do not report the amplitude. However, any nonlinearities arising from fluid or solid dynamic effects would alter the behavior of the amplitude versus frequency curves used to determine the quality factor and the experimental studies noted above were all in the linear regime.[5] Therefore, we will assume that $M \ll 1$.

For a wire undergoing a small amplitude displacement, the energy stored is $\mathrm{E}_{\mathrm{stored}}=k\langle A^2\rangle/2$ where the angle brackets indicate an average over the wire length and k is the restoring force constant. For $M \ll 1$, the fluid force per unit length on the wire can be assumed to be linearly related to the local velocity and is given by $F(z,t)=A(z)\omega[\zeta_R \sin(\omega t)+\zeta_I \cos(\omega t)]$. The coefficients ζ_R and ζ_I will in general depend on both the Knudsen number and the nondimensional oscillation frequency $\omega\tau_f$, where τ_f is the characteristic time for development of the gas flow. The fluid-phase dissipation is obtained by integrating the product of $F(z,t)$ and the local velocity of the wire over the wire length and over one period of the oscillation, yielding $\mathrm{E}^{\mathrm{f}}_{\mathrm{diss}}=\pi\zeta_R\langle A^2\rangle\omega L$. Since both the energy stored and the fluid dissipation are proportional to $\langle A^2\rangle$, the fluid contribution to the quality factor $Q^f=(2\pi\mathrm{E}_{\mathrm{stored}})/\mathrm{E}^{\mathrm{f}}_{\mathrm{diss}}$ is simply $k/(\zeta_R\omega L)$. Our study will focus on computing the damping coefficient ζ_R [in this paper, with dimensions mass/(length $\times$ time)] representing the ratio of the component of the force per unit length on the wire that is in phase with the velocity to the wire velocity.

The characteristic time τ_f for development of the gas flow depends on the Knudsen number. In the continuum regime, corresponding to $\mathrm{Kn} \ll 1$, $\tau_f=R^2/\nu$ is the time for diffusion of momentum over the characteristic length of the flow problem. In the free molecular flow regime, corresponding to $\mathrm{Kn} \gg 1$, $\tau_f=R/\langle c\rangle$ is the time for a gas molecule to propagate across the flow domain. For $\mathrm{Kn}=O(1)$, these two times are of the same order of magnitude. The values of $\omega\tau_f$ in the experimental studies vary from 10^{-3} to 10^{5}. The experimental study by Li *et al.*[7] is conducted entirely within the regime $\omega\tau_f \ll 1$ where one can apply a quasisteady drag coefficient. On the other hand the experimental study of Karabacak *et al.*[14] highlights the effects of unsteady flow for $\omega\tau_f=O(1)$. It should be noted, however, that the latter study varies the wire geometry and $\omega\tau_f$ simultaneously so that the trends seen may not be entirely attributable to the effects of unsteadiness in the gas flow.

Previous theoretical studies of gas-phase dissipation effects on vibrating wires have been limited and have mostly considered the continuum flow regime. Jeffrey and Onishi[16] solved the two-dimensional continuum Stokes flow driven by a cylinder translating normal to a planar surface. This provides a prediction of the drag coefficient in the quasisteady, continuum limit $\omega\tau_f \ll 1$ and $\mathrm{Kn}=0$. In Sec. III we will extend this theory to include the first noncontinuum flow effects for $\mathrm{Kn} \ll 1$ by applying a Maxwell slip boundary condition. Clarke *et al.*[17] studied the unsteady continuum flow driven by a vibrating cylinder for $\omega\tau_f=O(1)$ and $\mathrm{Kn}=0$. They also considered weak noncontinuum effects by using a Maxwell slip boundary condition, but only in the case where the cylinder is far from the wall $H \gg R$.

Bhiladvala and Wang[4] compared predictions of the quality factor including both solid and fluid dissipation with experimental measurements. Their treatment of the fluid dissipation neglected the interaction of the vibrating wire with the wall. Unsteady effects were incorporated only in the continuum regime. In the transition regime, they applied Yamamoto and Sera's[18] solution of the Bhatnagar–Gross–Krook (BGK) equation for steady translation of an isolated cylinder. The inertialess gas flow caused by a translating isolated cylinder does not decay with separation from the cylinder, a situation that is referred to as Stokes paradox in the continuum regime. Yamamoto and Sera's solution avoids Stokes paradox by including the gas inertia associated with the finite amplitude of the cylinder velocity. However, this resolution is inappropriate for $M \ll 1$. Bhiladvala and Wang's analysis produced the qualitative variation of quality factor with gas pressure observed in experimental studies but systematically underpredicted the dissipation. This underpredic-

tion could have resulted from the neglect of unsteady gas flow in the transition regime and/or the interactions with the bottom wall.

Yakhot and Colosqui[19] developed an approximate solution to the gas flow adjacent to a planar wall oscillating tangent to its surface in an unbounded noncontinuum gas and used this solution to discuss unsteady effects in vibrating nanowires. While this physical problem provides an illustration of unsteady transition gas flow effects, it does not directly model a vibrating nanowire in which the wire moves both tangent and normal to its surface, is nonplanar and interacts with a bounding surface. It should also be noted that Yakhot and Colosqui's analysis involves an expansion of the velocity distribution function for small deviations from the Maxwell distribution, which is not accurate at high frequencies. A complete solution of the kinetic problem for an oscillating planar wall is given by Sharipov and Kalempa[20] while the closely related problem of oscillatory planar Couette flow is treated in Refs. 21 and 22.

From our summary of the literature above, it is clear that significant discrepancies exist in the experimental literature for resonating nanowires and all theoretical attempts to understand this problem have either been restricted to a few asymptotic regimes of Kn or have only considered simplified versions of the problem. This paper is an attempt to bridge this gap using simulations as well as asymptotic theories to study drag on vibrating cylindrical nanowires. While our theories focus only on the quasisteady regime ($\omega\tau_f \ll 1$), we present simulation results for both quasisteady and unsteady flow conditions. In Sec. II we describe the geometry of the problem and discuss the newly developed low Mach number Bhatanagar–Gross–Krook direct simulation Monte Carlo (BGK-LM-DSMC) method[23] that will be used to simulate the gas flow driven by an oscillating cylinder. In Sec. III we develop theoretical predictions for the drag on the cylinder for quasisteady flows, $\omega\tau_f \ll 1$, in the slip $\mathrm{Kn} \ll 1$ and free molecular flow $\mathrm{Kn} \gg 1$ regimes. Section IV presents the simulation results comparing them with the asymptotic theories and with experimental results. The article ends with Sec. V where we summarize this work.

II. PROBLEM STATEMENT AND SIMULATION METHOD

We consider a cylinder of length L and radius R placed at a closest distance of approach H from the bottom surface (see Fig. 1). The cylinder oscillates in the vertical direction in a fluid with an average number density n_0 and an equilibrium temperature T, with a velocity $\mathbf{U}=U\sin(\omega t)\boldsymbol{e}_y$, where $U=A\omega$ with A and ω being the amplitude and frequency of oscillation. The distance between the cylinder center and the bottom wall is denoted by $d=R+H$. As discussed in Sec. I, aspect ratios of the nanowires studied in the experimental literature are large thus allowing us to treat a local quasi-two-dimensional flow problem where we neglect the spatial variations along the length of the cylinder. The fluid dissipation will be analyzed in terms of either the drag force per unit length or the damping coefficient defined earlier. As noted, oscillation amplitudes in these experiments can be assumed

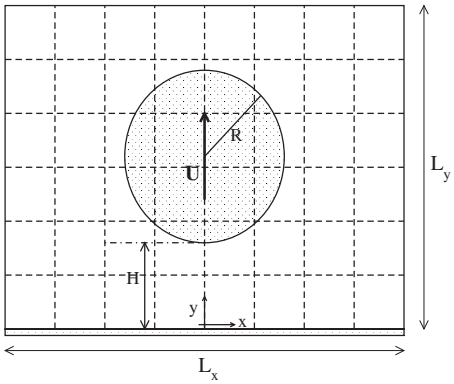

FIG. 1. Simulation domain.

to be small enough so that the Mach number $M \ll 1$ and the nanowire position remains unchanged both in our theory and during the course of simulation.

To set the stage for our simulation method, we briefly review the Boltzmann formulation for rarefied gas flows. Let $n(\mathbf{r},t)$ and $f=f(\mathbf{c},\mathbf{r},t)$ represent the number density and the velocity distribution function, respectively, at spatial position $\mathbf{r}$ and time t with $\mathbf{c}$ denoting the molecular velocity. The space-time evolution of the probability density function nf is given by the Boltzmann equation

$$\frac{\partial(nf)}{\partial t} + \mathbf{c}\cdot\frac{\partial(nf)}{\partial \mathbf{r}} = \left[\frac{\partial(nf)}{\partial t}\right]_{\mathrm{coll}}. \tag{3}$$

The term on the right hand side of the equation is the collision operator that represents the change in the density function due to intermolecular collisions. The exact collision operator is nonlinear and involves integrals over velocity space of products of the velocity distributions of colliding molecules. At solid boundaries, molecules can be assumed to undergo diffuse or specular reflection or a combination of both.[24] In this study, we consider only diffuse reflection from all solid surfaces. In the case of open boundaries that are in contact with an equilibrium reservoir of gas moving with an average velocity relative to the boundary, outgoing molecules are assumed to permanently leave the domain while incoming molecules are assumed to enter the domain with a distribution matching that of the reservoir. At equilibrium, $[\partial(nf)/\partial t]_{\mathrm{coll}}=0$ and in the absence of any external forces and moving boundaries, solving Eq. (3) yields a number density, $n(\mathbf{r},t)=n_0$, that is uniform and a velocity distribution function that is given by a Maxwell–Boltzmann distribution,

$$f_{MB}(\mathbf{c}) = \left(\frac{m}{2\pi k_B T}\right)^{3/2}\exp\left(-\frac{m\mathbf{c}^2}{2k_B T}\right). \tag{4}$$

In the presence of external forces and moving boundaries, Eq. (3) can be solved analytically only for simple geometries and by applying a suitable approximation for the collision term. One such approximation is the BGK approximation,[25] in which the right hand side in Eq. (3) is approximated as a linear function of the deviation from local equilibrium,

$$\left[\frac{\partial(nf)}{\partial t}\right]_{\text{coll}} = \frac{\{n(\mathbf{r})f_{MB}[\mathbf{c}-\mathbf{u}(\mathbf{r})]-n(\mathbf{r})f(\mathbf{c})\}}{\tau}, \tag{5}$$

where $n(\mathbf{r})$ is a local number density and $\mathbf{u}(\mathbf{r})$ represents a locally averaged flow velocity. τ is a free parameter and is typically chosen so that the viscosity of the fluid satisfies the known result $\eta=(1/2)mn_0\langle c\rangle\lambda$, yielding $\tau=(4/\pi)(\lambda/\langle c\rangle)$. The BGK approximation is based on the idea that the rate at which collisions drive the distribution function toward the *local* equilibrium value depends linearly on the deviation from local equilibrium.

The Boltzmann equation and its approximate versions can be solved analytically only for simple geometries. For more complex situations such as the one we are dealing with in this article, one needs to turn to a simulation based approach. One such technique is the DSMC, a coarse-grained particle-based stochastic simulation method developed by Bird,[24] that attempts to replicate the effects of the Boltzmann equation (3). In this method, a single simulation particle is used to represent a large integer number N_m of gas molecules thus reducing the number of degrees of freedom considerably. The velocity distribution of the particles directly represents the molecular velocity distribution even when the latter deviates from equilibrium. The effects of advection and acceleration by an external force on particle positions and velocities are treated in a deterministic manner. Intermolecular collisions are determined based on kinetic theory and are treated in a probabilistic manner. Two DSMC simulation particles do not have to strictly come in contact with each other for an intermolecular collision to occur. Instead particles within a spatial cell are chosen to collide based on collision rates derived from kinetic theory. All averaged quantities are computed directly by ensemble averaging over functions of particle velocities. For more details on the DSMC method, we refer the reader to Ref. 24. The DSMC method has been successfully applied to high speed rarefied gas flows ($M \geq 0.2$). However, as emphasized in Refs. 23 and 26, flow speeds in nanoscale applications, such as is relevant here, are typically very small and, consequently, results from DSMC simulations of such systems are dominated by statistical noise thus rendering the technique very inefficient and in some cases completely useless.

We therefore turn to our newly developed BGK-LM-DSMC simulation method,[23] an efficient modified DSMC algorithm that simulates the linearized BGK approximation to the Boltzmann equation. Here, each simulation particle is assumed to represent $N_m(1+MW_i)$ molecules where M, as before, represents the Mach number and W_i represents a variable noninteger particle weighting. Unlike the regular DSMC method, particle velocities are always representative of equilibrium thermal velocities and all effects of external forces and moving boundaries are reflected in the $O(M)$ particle weightings. When particles undergo diffuse reflections from solid boundaries, their weightings are updated according to a certain set of rules which are described below. Interparticle collisions are replaced with a BGK type relaxation in which a chosen fraction of particles is allowed to relax toward the local equilibrium by suitably modifying their weightings. Mean quantities are computed by performing a weighted average over particle velocities. Although the simulation method is very general and can be used to study low speed flow in any geometry, below, we present some of the details of the simulation method in the context of the nanowire problem. It should be emphasized that a thorough description of the method is beyond the scope of this article and for more details we refer the reader to our earlier publication[23] where we have also documented the success of this method in studying test problems for which analytical results are available.

As shown in Fig. 1, we consider a cylinder of radius R placed near a wall at a distance of closest approach H. The simulation domain is bounded by a box whose dimensions are chosen such that they are at least a few mean free paths larger than $H+2R$. The box dimensions were increased until convergent results were obtained. The simulation domain is first divided into cells where the maximum linear dimension of each cell L_c is chosen such that it is smaller than both the mean free path and the smallest characteristic length scale in the problem, i.e., $L_c < \min[\lambda, \min(R,H)]$. We use about $N=50$ simulation particles per cell which ensures that the local velocity distribution function is represented with sufficient accuracy. The integration time step Δt is chosen to be equal to $(L_c/\langle c\rangle)/4$—small enough such that the particle moves only a fraction of the cell length in each time step. The choice of these parameters is similar to that for the standard DSMC method discussed in Ref. 27.

At the beginning of the simulation, particles are initialized at random positions with velocities chosen from the Maxwell distribution. Every time step in the simulation can be decomposed into a propagation step and a collision step. During the propagation step, the position of the particle is updated according to $\mathbf{r}_i(t+\Delta t)=\mathbf{r}_i+\mathbf{c}_i(t)\Delta t$, where $\mathbf{r}_i(t)$ and $\mathbf{r}_i(t+\Delta t)$ represent positions of particle i at the beginning and end of the time step and $\mathbf{c}_i(t)$ represents the velocity of particle i at the beginning of the time step. If the particle crosses the bottom wall or the surface of the nanowire during the time step, the time of intersection with the boundary is determined using geometry. The particle is assumed to undergo diffuse reflection from these surfaces and a new particle velocity is chosen from an equilibrium distribution while ensuring that diffuse reflection rules are obeyed. The particle is allowed to propagate for the remainder of the time step with the new velocity. In addition to the velocities, the weightings of the particles also need to be updated. Whereas the weightings of the particles reflecting off the bottom surface remain unchanged, the weightings of the particles reflecting off the moving nanowire are given by[23]

$$W_i(t+\Delta t) = W_i(t) + 2\mathbf{n}_1 \cdot \mathbf{U}^* + \frac{8}{\pi}\mathbf{U}^* \cdot \mathbf{c}_i^*, \tag{6}$$

where $\mathbf{U}^*=\mathbf{U}/U$ is the nondimensionalized velocity of the nanowire boundary, $\mathbf{n}_1$ is the unit normal to the nanowire at the point of collision of the particle with the surface, and $\mathbf{c}_i^*=\mathbf{c}_i/\langle c\rangle$ represents the dimensionless particle velocity. Whereas both the incoming and reflected particles have an unweighted equilibrium velocity distribution, these updated weightings assure that the weighted velocity distribution

function reflects the nonequilibrium effects of the moving boundary. For unsteady simulations the nanowire velocity is given by $\mathbf{U}=U\sin(\omega t)\boldsymbol{e}_y$ whereas for quasisteady simulations, it is given by $\mathbf{U}=U\boldsymbol{e}_y$. At the outer boundary of the simulation domain, we apply a boundary condition in which the simulation domain is assumed to be in equilibrium with a reservoir of gas whose number density and velocity is given by Jeffrey and Onishi's[16] continuum solution outlined in Sec. III A. As explained in Ref. 23, such a boundary condition offers improved convergence when compared to a boundary condition in which the simulation domain is assumed to be in equilibrium with a stationary gas reservoir. The Jeffrey–Onishi boundary condition is implemented by ensuring that any time a particle strikes the outer boundary, it is specularly reflected back into the simulation domain with a postreflection weighting given by[23]

$$W_i = \frac{8}{\pi}\mathbf{u}^* \cdot \mathbf{c}_i^* + \frac{p}{Mn_0 k_B T}, \tag{7}$$

where $\mathbf{u}^*$ is the fluid velocity nondimensionalized by U and p is the pressure. $\mathbf{u}^*$ and p are both evaluated at the point of contact between the particle and the outer boundary using Jeffrey and Onishi's solution.[16] As noted by Gopinath and Koch,[28] far-field flow driven by a moving finite Kn particle can be approximated as continuum provided it is based on the force that the particle exerts on the fluid. This is based on the observation that the integral of the stress exerted on a fluid boundary that encloses a particle is equal to the force exerted by the particle on the fluid. This argument is strictly valid when the surface enclosing the particle does not intersect the wall. However, we used the continuum flow including wall effects due to a cylinder exerting the force determined from the simulation and found that this scheme gives good convergence as the size of the outer boundary is increased. Hence, we use Eq. (22) to evaluate the coefficient D_1 in Jeffery and Onishi's solution in terms of the cylinder force computed from the simulation. The other coefficients in the continuum flow solution can then be determined using Eq. (21). The drag force per unit length $\mathbf{F}$ in Eq. (22) is computed as an averaged quantity during the course of the simulation via

$$\mathbf{F} = \frac{MN_m m\langle \Sigma_{\text{in}} W_i \mathbf{c}_i - \Sigma_{\text{out}} W_i \mathbf{c}_i \rangle}{\Delta t}, \tag{8}$$

where Σ_{in} and Σ_{out} represent sums over all particles arriving at and leaving the surface, respectively, thus yielding a self-consistent simulation method. For quasisteady flows, $\mathbf{F}$ is averaged over several fluid equilibration times in order to obtain the average drag force on the nanowire, while the damping coefficient is averaged over a similar time period for unsteady flows. Figure 2, which shows results for the average dimensionless quasisteady drag force as a function of simulation box size, L_{box}, for a system with $H/R=1.8182$, confirms that our results are not affected by the finite size of the simulation cell.

The collision step of the BGK-LM-DSMC method differs significantly from that in the standard DSMC method. Unlike standard DSMC where pairs of particles collide during a collision step, in the BGK-LM-DSMC method, particle velocities are unchanged and particle weightings are modified independent of each other in a manner consistent with the BGK relaxation process as we now describe. At every time step, a number $N_B=f_B N$ of the N particles in the cell are randomly chosen to relax toward local equilibrium where $f_B=1-\exp(-\Delta t/\tau)$ represents the fraction of molecules undergoing relaxation during a time step Δt. The postrelaxation weightings of these chosen particles are given by[23]

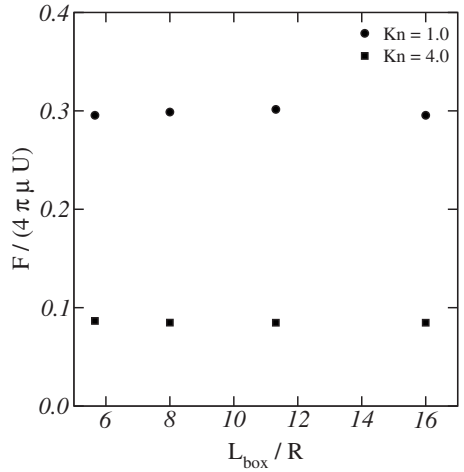

FIG. 2. Convergence of drag force results with simulation box size for a system with $H/R=1.8182$.

$$W_i^{>} = \langle W \rangle_c + \frac{8}{\pi}\mathbf{c}_i^* \cdot \langle \mathbf{u} \rangle_c^*, \tag{9}$$

where $\mathbf{c}_i^*=\mathbf{c}_i/\langle c \rangle$ is the nondimensionalized particle velocity and $\langle \mathbf{u} \rangle_c^*=\langle \mathbf{u} \rangle_c/U$ is the nondimensionalized cell-averaged velocity. $\langle W \rangle_c$ and $\langle \mathbf{u} \rangle_c^*$, the cell-averaged particle weighting and fluid velocity, are given by

$$\langle W \rangle_c = \frac{\Sigma_{N-N_B} W_i}{N-N_B}, \qquad \langle \mathbf{u} \rangle_c^* = \frac{\Sigma_{N-N_B} W_i \mathbf{c}_i^*}{N-N_B}, \tag{10}$$

where the averages are defined such that they only include those particles in the cell that have not been chosen to undergo relaxation during that particular time step. This process of averaging over only the nonrelaxing particles in the cell ensures that there are no correlations between the pre- and postrelaxation weightings of particles. As discussed in Ref. 23, the BGK relaxation process does not conserve momentum and energy exactly at every time step but does so only in an average sense. To improve statistical accuracy, we strictly enforce conservation of mass, momentum, and energy at every time step by adjusting the postrelaxation weightings of all particles in the cell according to the procedure described in Ref. 23.

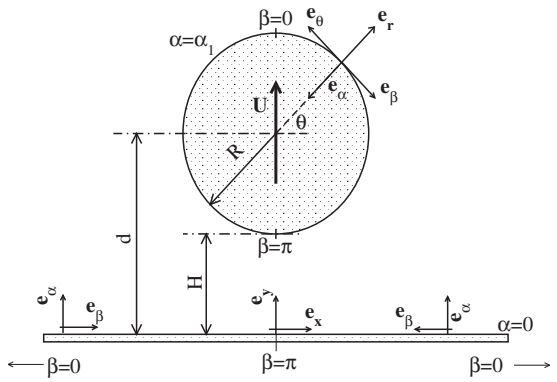

FIG. 3. Problem geometry.

III. THEORY FOR QUASISTEADY DRAG FORCE

In this section, we present analytical predictions for the drag force per unit length acting on an infinite cylinder moving perpendicular to a wall. The analysis is limited to the quasisteady regime where $\omega\tau_f \ll 1$ with ω and τ_f, as defined before, being the oscillation frequency and the characteristic fluid relaxation time, respectively. We begin by reviewing Jeffrey and Onishi's[16] theory for the continuum regime (Kn=0). In Sec. III B, we extend the Jeffrey–Onishi analysis to obtain the first noncontinuum effects on the drag for $\mathrm{Kn} \ll 1$ by applying slip boundary conditions at the wall and on the surface of the cylinder. Finally, in Sec. III C, we present our theoretical results for the drag force in the free molecular flow regime, $\mathrm{Kn} \gg 1$.

A. Continuum regime (Kn=0)

Jeffrey and Onishi[16] solved for the drag force on a cylinder translating normal to a wall by expressing the problem in bipolar coordinates (α,β) (see Fig. 3) which can be written in terms of Cartesian coordinates (x,y) according to

$$xh = \sin\beta, \tag{11a}$$

$$yh = \sinh\alpha, \tag{11b}$$

where $ah = \cosh\alpha - \cos\beta$ with $a = \sqrt{d^2 - R^2}$. The flow is described by the Stokes equation

$$\nabla^4\psi = 0, \tag{12}$$

with ψ representing the stream function, in terms of which the velocity components are defined as

$$u_\alpha = -h\frac{\partial\psi}{\partial\beta}, \qquad u_\beta = h\frac{\partial\psi}{\partial\alpha}. \tag{13}$$

The general solution for ψ is given by

$$h\psi = \mathrm{Re}\left[\sum_{n=0}^{\infty}\chi_n(\alpha)e^{-\imath n\beta}\right], \tag{14}$$

where "Re" denotes the real part of the expression and χ_n are complex coefficients with

$$\begin{aligned}
\chi_0 &= A_0\cosh\alpha + B_0\alpha\cosh\alpha + C_0\sinh\alpha + D_0\alpha\sinh\alpha,\\
\chi_1 &= A_1\cosh 2\alpha + B_1 + C_1\sinh 2\alpha + D_1\alpha,\\
\chi_n &= A_n\cosh(n+1)\alpha + B_n\cosh(n-1)\alpha\\
&\quad + C_n\sinh(n+1)\alpha + D_n\sinh(n-1)\alpha.
\end{aligned} \tag{15}$$

The pressure field is given by

$$p = \frac{2\mu}{a}\mathrm{Im}\left[e^{-\imath\beta}\{D_0\sinh\alpha + (B_0+D_1)\cosh\alpha\} + \sum_{n=1}^{\infty}e^{-\imath n\beta}\{G_n\sinh n\alpha + H_n\cosh n\alpha\}\right], \tag{16}$$

where

$$\begin{aligned}
G_n &= (n-1)(A_{n-1}+B_n) - (n+1)(A_n + B_{n+1}),\\
H_n &= (n-1)(C_{n-1}+D_n) - (n+1)(C_n + D_{n+1}).
\end{aligned} \tag{17}$$

On applying no-penetration and no-slip boundary conditions on the bottom wall $(\alpha=0)$ and the cylinder $(\alpha=\alpha_1)$, no-penetration:

$$\begin{aligned}
u_\alpha &= 0, \quad \text{at} \quad \alpha = 0,\\
u_\alpha &= -U\sin\theta, \quad \text{at} \quad \alpha = \alpha_1,
\end{aligned} \tag{18}$$

no-slip:

$$\begin{aligned}
u_\beta &= 0, \quad \text{at} \quad \alpha = 0,\\
u_\beta &= U\cos\theta, \quad \text{at} \quad \alpha = \alpha_1,
\end{aligned} \tag{19}$$

where α_1 is obtained from the relation $R\sinh\alpha_1 = a$ and θ represents the azimuthal coordinate in the polar coordinate system (r,θ) which is related to the Cartesian coordinate system via

$$x = r\cos\theta, \tag{20a}$$

$$y = r\sin\theta. \tag{20b}$$

The only nonvanishing coefficients are purely imaginary and are given by

$$\begin{aligned}
2A_1\coth\alpha_1 &= -2B_1\coth\alpha_1\\
&= -2C_1 = D_1 = \imath U/(\alpha_1 - \tanh\alpha_1).
\end{aligned} \tag{21}$$

Using Eqs. (21), (14), and (13), one can obtain the velocity field and the corresponding gradients. These gradients can be used to determine the stress field $\boldsymbol{\sigma}$, which on integrating over the cylinder surface dS_1 yields the drag force per unit length on the cylinder,

$$\mathbf{F} = \int dS_1\boldsymbol{\sigma}\cdot\mathbf{n}_1 = 4\pi\mu(D_0\boldsymbol{e_x} - \mathrm{Im}\{D_1\}\boldsymbol{e_y}). \tag{22}$$

Here $\mathbf{n}_1$ is the normal to the cylinder at any given point and $\boldsymbol{e_x}$ and $\boldsymbol{e_y}$ are unit vectors in the Cartesian coordinate system. Using the value for D_1 given in Eq. (21), Jeffrey and Onishi evaluated the nondimensionalized drag force per unit length acting on the cylinder to be

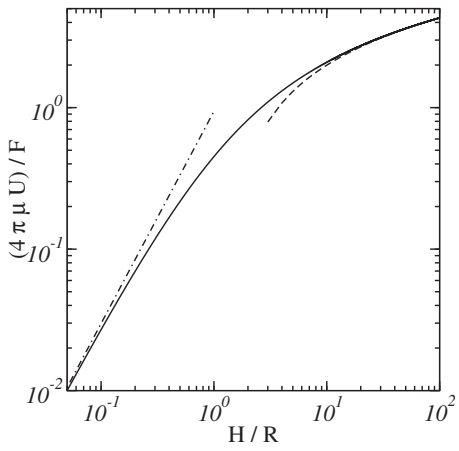

FIG. 4. Dimensionless inverse drag force per unit length as a function of dimensionless distance between nanowire and bottom wall for continuum (Kn=0) flow. The solid line is obtained by using Eq. (23), the dotted-dashed line represents lubrication theory results for small H/R given in Eq. (24), and the dashed line represents the approximation for $H/R \gg 1$ given in Eq. (25).

$$\frac{F}{4\pi\mu U} = \frac{1}{\ln\left[\frac{d+a}{R}\right] - \frac{a}{d}}. \tag{23}$$

This result is plotted in Fig. 4. For $H/R \ll 1$, a lubrication type calculation yields[16]

$$\frac{F}{4\pi\mu U} = 3\left(2\frac{H}{R}\right)^{-3/2}, \tag{24}$$

while for $H/R \gg 1$, Eq. (23) simplifies to

$$\frac{F}{4\pi\mu U} = \frac{1}{\ln\left(2\frac{H}{R}\right) - 1}. \tag{25}$$

Both these results are also shown in Fig. 4. For continuum and low Kn finite Re flows, the drag force is given by

$$\frac{F}{4\pi\mu U} = \frac{1}{\ln\left(\frac{1}{\mathrm{Re}}\right) + K_1}, \tag{26}$$

where, for continuum flows, $K_1 = \ln(7.4)$ (Ref. 29) and, for finite Knudsen flows, K_1 depends on Kn as given in Ref. 18. On comparing Eqs. (25) and (26), we note that for finite Re flows, $R\,\mathrm{Re}^{-1}$ replaces H as a cutoff length which can be true only if $H \gg \nu/U$.

B. Slip regime (Kn≪1)

At small but nonzero Kn, the presence of a thin layer of $O(\lambda)$ near a boundary influences the nearby viscous layer significantly. In such a case, the fluid at the boundary has a velocity different from the boundary itself.[30] This effect can be captured by approximating the fluid to be slipping past the boundary with a slip velocity which is assumed to be proportional to the velocity gradient.

To compute the drag force in the slip regime, we solve the Stokes flow problem, Eq. (12) but now with no-penetration and *slip* boundary conditions being satisfied on the bottom wall ($\alpha=0$) and the cylinder surface ($\alpha=\alpha_1$), no-penetration:

$$\begin{aligned} u_\alpha &= 0, \quad \text{at} \quad \alpha = 0, \\ u_\alpha &= -U\sin\theta, \quad \text{at} \quad \alpha = \alpha_1, \end{aligned} \tag{27}$$

slip:

$$\begin{aligned} u_x &= \gamma\frac{\partial u_x}{\partial y} \Rightarrow u_\beta = \gamma\frac{\partial u_\beta}{\partial\alpha}\frac{\partial\alpha}{\partial y}, \quad \text{at} \quad \alpha = 0 (y = 0), \\ u_\theta - U\cos\theta &= \gamma\frac{\partial u_\theta}{\partial r} \Rightarrow u_\beta - U\cos\theta \\ &= \gamma\frac{\partial u_\beta}{\partial\alpha}\frac{\partial\alpha}{\partial r}, \quad \text{at} \quad \alpha = \alpha_1 (r = R), \end{aligned} \tag{28}$$

where u_r and u_θ represent the components of the fluid velocity in the polar coordinate system, and u_x and u_y the components of fluid velocity in the Cartesian coordinate system. $\gamma = 1.1466\lambda$ is the slip coefficient.[31] The derivatives $(d\alpha/dr)_{\alpha=\alpha_1}$ and $(d\alpha/dy)_{\alpha=0}$ are obtained by differentiating the coordinate definition Eqs. (13) and (22) with respect to r and y and rearranging terms. The general form of the solution to the Stokes problem continues to be given by Eqs. (14) and (15), where we assume $\chi_0 = 0$ and χ_n are all purely imaginary. We consider N terms in the summation in Eq. (14) with N chosen to be large enough so that the solution converges.

For $\mathrm{Kn} \ll 1$, γ/R is also much smaller than 1, and hence we can write the stream function as a linear function of γ/R, $\psi = \psi^{(0)} + (\gamma/R)\psi^{(1)}$. Similar linear expansions can be used for other unknowns in this problem, i.e., u_α, u_β, χ_n, A_n, B_n, C_n, and D_n. After substituting these linearization approximations in Eqs. (13)–(15) and applying boundary conditions (27) and (28), two different sets of equations are obtained by comparing terms of different orders in γ/R. The $O((\gamma/R)^0)$ terms lead to one set of equations, which, on solving, yield the zeroth order terms, i.e., terms with superscript (0). The zeroth order solution is found to be identical to the Jeffrey–Onishi solution for the no-slip problem outlined in the previous section. The $O[(\gamma/R)^1]$ terms yield a system of $4N \times 4N$ linear equations for the coefficients $A_n^{(1)}$, $B_n^{(1)}$, $C_n^{(1)}$, and $D_n^{(1)}$ $(n = 1 \cdots N)$ which has to be solved numerically. As explained in Sec. III A, the coefficients, once solved for, can be used to determine the velocity and stress fields from which the drag force can be computed.

The final solution for the drag force can also be expressed as a linear function of Kn,

$$F = F^{(0)} + \mathrm{Kn}F^{(1)}, \tag{29}$$

where $F^{(0)}$ is the Jeffrey–Onishi continuum drag force given

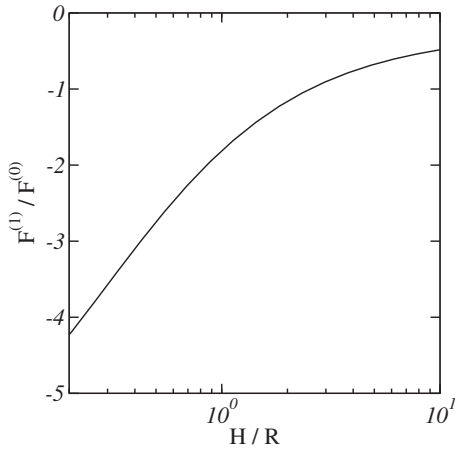

FIG. 5. Nondimensionalized slip correction to the drag force, $F^{(1)}/F^{(0)}$, plotted as a function of dimensionless distance between nanowire and bottom wall.

by Eq. (23) and $F^{(1)}$ represents a correction due to slip. In Fig. 5, we show a plot of this correction term as a function of the distance of the nanowire from the bottom wall. The slip correction is negative over the entire range of H/R indicating that drag in the slip regime is smaller than in the continuum regime. The correction increases with decreasing distance and diverges for $H/R \ll 1$ because, in this regime, lubrication theory indicates that the shear rate in the gap will diverge as $U(R/H^2)$ and this large shear rate induces a large slip. It should also be noted that the slip flow lubrication solution requires $\lambda/H \ll 1$ which is much more restrictive than $\mathrm{Kn}=\lambda/R \ll 1$. A detailed discussion of noncontinuum lubrication theory for the case $\lambda/H \sim O(1)$ can be found in Ref. 32.

C. Free molecular flow regime (Kn≫1)

For the free molecular flow regime, we compute the drag force on the nanowire using an approach similar to that described in Refs. 33 and 34. In this regime, the mean free path is assumed to be large enough that intermolecular collisions can be neglected. The net force exerted by the gas molecules on the nanowire is given by

$$\mathbf{F} = \int_{S_1} dS_1 d\mathbf{F}_1(\mathbf{r}_1), \tag{30}$$

where subscript 1 is used to denote the nanowire and the integral is carried out over the entire surface of the nanowire S_1. $d\mathbf{F}_1$, the average force per unit area acting at any particular point $\mathbf{r}_1$ on the nanowire's surface, is given by $d\mathbf{F}_1(\mathbf{r}_1) = d\mathbf{F}_1{}^-(\mathbf{r}_1) - d\mathbf{F}_1{}^+(\mathbf{r}_1)$, where $d\mathbf{F}_1{}^+(\mathbf{r}_1)$ is the rate at which momentum is transferred away from the surface by reflected molecules and $d\mathbf{F}_1{}^-(\mathbf{r}_1)$ is the rate at which momentum is transferred to the surface by incident molecules,

$$d\mathbf{F}_1{}^+(\mathbf{r}_1) = -n_1(\mathbf{r}_1)\int_{(\mathbf{c}-\mathbf{U})\cdot\mathbf{n}_1>0} d\mathbf{c} m\mathbf{c}|(\mathbf{c}-\mathbf{U})\cdot\mathbf{n}_1| f_{MB}(\mathbf{c}-\mathbf{U}), \tag{31}$$

$$d\mathbf{F}_1{}^-(\mathbf{r}_1) = n_0\int_{(\mathbf{c}-\mathbf{U})\cdot\mathbf{n}_1<0} d\mathbf{c} m\mathbf{c}|(\mathbf{c}-\mathbf{U})\cdot\mathbf{n}_1| f_{MB}(\mathbf{c}) + \int_{\Omega_{21}} d\mathbf{c} n_2(\mathbf{r}_2) m\mathbf{c}|(\mathbf{c}-\mathbf{U})\cdot\mathbf{n}_1| f_{MB}(\mathbf{c}) - n_0\int_{\Omega_{21}} d\mathbf{c} m\mathbf{c}|(\mathbf{c}-\mathbf{U})\cdot\mathbf{n}_1| f_{MB}(\mathbf{c}).$$

Here, $\mathbf{n}_1$ is the outward normal to the cylinder at point $\mathbf{r}_1$ and $\int_{\Omega_{21}} d\mathbf{c}$ is an integral over only those velocity vectors that emanate from the wall and end at point $\mathbf{r}_1$. This integral reflects the extra force exerted on the wire because the number density of molecules reflected off the bottom wall exceeds the equilibrium value. The flux of molecules emitted by the cylinder (bottom wall) is equivalent to that produced by a half space of gas with number density $n_1(\mathbf{r}_1)$ $[n_2(\mathbf{r}_2)]$ and velocity distribution $f_{MB}(\mathbf{c}-\mathbf{U})$ $[f_{MB}(\mathbf{c})]$. The only unknowns in the above equations, $n_1(\mathbf{r}_1)$ and $n_2(\mathbf{r}_2)$, can be determined by applying the constraint that mass must be strictly conserved at every point on the cylinder as well as on the wall, i.e., on any object i with $i=1$ representing the cylinder and $i=2$ representing the bottom wall., the outgoing flux of molecules $j_i^+(\mathbf{r}_i)$ should equal the incoming flux of molecules $j_i^-(\mathbf{r}_i)$,

$$j_i^+(\mathbf{r}_i) = j_i^-(\mathbf{r}_i). \tag{32}$$

These fluxes are given by

(i) Cylinder:

$$j_1^+(\mathbf{r}_1) = n_1(\mathbf{r}_1)\int_{(\mathbf{c}-\mathbf{U})\cdot\mathbf{n}_1>0} d\mathbf{c}|(\mathbf{c}-\mathbf{U})\cdot\mathbf{n}_1| f_{MB}(\mathbf{c}-\mathbf{U}), \tag{33}$$

$$j_1^-(\mathbf{r}_1) = n_0\int_{(\mathbf{c}-\mathbf{U})\cdot\mathbf{n}_1<0} d\mathbf{c}|(\mathbf{c}-\mathbf{U})\cdot\mathbf{n}_1| f_{MB}(\mathbf{c}) + \int_{\Omega_{21}} d\mathbf{c} n_2(\mathbf{r}_2)|(\mathbf{c}-\mathbf{U})\cdot\mathbf{n}_1| f_{MB}(\mathbf{c}) - n_0\int_{\Omega_{21}} d\mathbf{c}|(\mathbf{c}-\mathbf{U})\cdot\mathbf{n}_1| f_{MB}(\mathbf{c}).$$

(ii) Wall:

$$j_2^+(\mathbf{r}_2) = n_2(\mathbf{r}_2)\int_{\mathbf{c}\cdot\mathbf{n}_2>0} d\mathbf{c}|\mathbf{c}\cdot\mathbf{n}_2| f_{MB}(\mathbf{c}), \tag{34}$$

$$j_2^-(\mathbf{r}_2) = n_0\int_{\mathbf{c}\cdot\mathbf{n}_2<0} d\mathbf{c}|\mathbf{c}\cdot\mathbf{n}_2| f_{MB}(\mathbf{c}) + \int_{\Omega_{12}} d\mathbf{c} n_1(\mathbf{r}_1) \times|\mathbf{c}\cdot\mathbf{n}_2| f_{MB}(\mathbf{c}-\mathbf{U}) - n_0\int_{\Omega_{12}} d\mathbf{c}|\mathbf{c}\cdot\mathbf{n}_2| f_{MB}(\mathbf{c}).$$

Here, $\mathbf{n}_2$ is the outward normal to the wall at point $\mathbf{r}_2$ and $\int_{\Omega_{12}} d\mathbf{c}$ is an integral over only those velocity vectors that

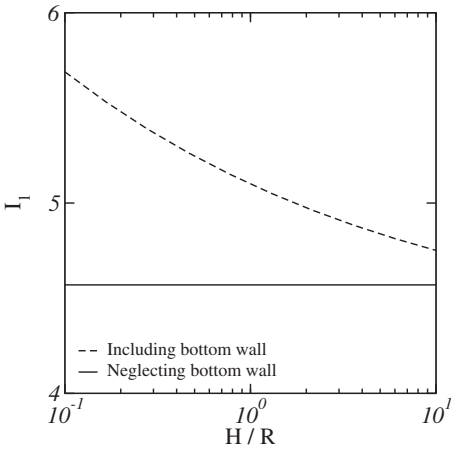

FIG. 6. I_1 as a function of dimensionless distance between nanowire and bottom wall.

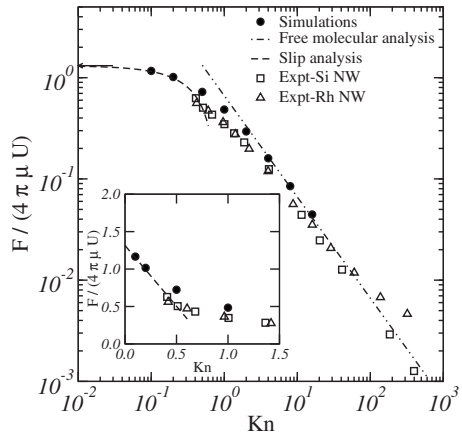

FIG. 7. Drag force per unit length as a function of Knudsen number for $H/R=1.8182$ corresponding to dimensions reported in Ref. 7. Legends are as shown in figure. Arrow near the y-axis represents the Jeffrey–Onishi predictions in the continuum limit Kn=0. The inset shows the same data on a linear-linear scale (free molecular flow results omitted for clarity). For simulations, error bars are smaller than symbol size.

emanate from the cylinder and end at point $\mathbf{r}_2$. For small Mach numbers, as is relevant here, we can approximate n_1, n_2, and $f_{MB}(\mathbf{c}-\mathbf{U})$ as linear functions of the Mach number M,

$$n_1 = n_0[1 + M\nu_1(\mathbf{r}_1)],$$

$$n_2 = n_0[1 + M\nu_2(\mathbf{r}_2)], \tag{35}$$

$$f_{MB}(\mathbf{c}-\mathbf{U}) = f_{MB}(\mathbf{c})\left(1 + \frac{m}{k_B T}\mathbf{c}\cdot\mathbf{U}\right)$$

$$= f_{MB}(\mathbf{c})\left(1 + \frac{8}{\pi}M\mathbf{c}^*\cdot\mathbf{U}^*\right).$$

Here, $\mathbf{U}^*=\mathbf{U}/U$ and $\mathbf{c}^*=\mathbf{c}/\langle c\rangle$ are the dimensionless nanowire and gas molecule velocities, respectively. On substituting these approximations into Eqs. (33) and (34) and keeping terms of only $O(M)$, we obtain linear integral equations for ν_1 and ν_2 which are then solved numerically. The numerical solution involves defining grids on the surfaces of both the cylinder and the wall and applying Simpson's rule to discretize the integrals. Applying a similar linearization procedure to Eqs. (30) and (31) allows us to express the average force on the nanowire as a function of the perturbations ν_1 and ν_2. The final expression for the nondimensionalized average drag force per unit length acting on the cylinder is given by

$$\frac{F}{4\pi\mu U} = \frac{I_1}{8\mathrm{Kn}}, \tag{36}$$

where I_1 is a functional of ν_1 and ν_2 integrated over both $\mathbf{r}_1$ and $\mathbf{r}_2$ and thus indirectly depends on system geometry. Figure 6 shows how I_1 varies with H/R. We also show values for I_1 for an isolated nanowire, i.e., in the absence of the bottom wall, which can be obtained using a method similar to the one described above, and the final result for which is given by $I_1=0.5(6+\pi)=4.57$.[34] I_1 in the presence of the bottom wall is higher than that for an isolated cylinder indicating that the existence of the bottom wall leads to higher drag forces. At the smallest separations explored, the drag force can be nearly 25% larger. As the separation between the nanowire and the wall increases, I_1 and hence the drag force decreases, approaching predictions for the isolated cylinder at large H/R.

IV. DISCUSSION

In this section, we summarize the results of our theoretical analysis and our BGK-LM-DSMC simulations. Wherever possible, we also compare our results with some relevant experimental data. Section IV A focuses on the quasisteady regime while Sec. IV B focuses on the unsteady regime.

A. Quasisteady regime ($\omega\tau_f \ll 1$)

In Fig. 7, we plot the nondimensionalized drag force per unit length as a function of Knudsen number Kn. The gap between the wire and the wall was set as $H/R=1.8182$, which corresponds to the rest position of the wire used in Ref. 7. Our simulations indicate that the drag force increases with decreasing Kn and smoothly rolls over to a Kn independent value at low values of Kn. In the same figure, we also show results from our free molecular flow calculations [Eq. (36)], the slip theory (Sec. III B and the Jeffrey–Onishi predictions for continuum flow [Eq. (23)]) for the system under consideration. For the free molecular flow limit, our numerical analysis yields $I_1=4.99$ in Eq. (36). It should be noted that, for an isolated nanowire where the bottom wall is absent, a similar analysis yields $I_1=0.5(6+\pi)=4.57$.[34] Thus, the interaction with the wall increases the drag by about 10% for $H/R=1.8182$.

The enhancement in drag due to wall interactions will increase with decreasing H/R. As seen from the figure, at high Kn ($\mathrm{Kn}\geq 1$), the simulations approach the asymptotic value predicted by our free molecular analysis and at low Kn ($\mathrm{Kn}\leq 0.1$), our simulations agree with predictions of our theoretical slip calculations. As expected, both the simulations and the slip theory approach the continuum predictions (shown as an arrow in the figure) at low Kn.

The theory/simulation results are compared with experimental data from Li *et al.*[7] This particular experimental data set is useful for comparison because of its relevance to the quasisteady regime considered, as well as the careful inclusion of relevant parameters. The authors introduce a hybrid bottom-up technique, using electrofluidic directed-assembly of silicon and rhodium nanowires and electrodeposited clamps to create large arrays of cantilevered nanoresonators. Cross-talk between resonators and clamp losses associated with support undercuts were removed and the electrodeposition process was shown to produce clamps of repeatable rigidity. The nanowires in the array were separated by distances much larger than their diameters and thus any form of interaction between these nanowires can be neglected. The data used here are for a silicon nanowire with a length of 11.8 μm and diameter 330 nm and for a rhodium nanowire of length 5.8 μm and diameter 280 nm. The cantilevered nanowires were suspended with a 300 nm gap from the bottom surface. The nanowire chip was mounted in a vacuum chamber where ambient gas pressure of pure dry nitrogen gas was varied from 10^{-10} to 1 atm. The nanowires were driven using a tip fringe field electrostatic drive and a laser interferometry technique was used to obtain the resonance spectrum, from which the Q-factor at each pressure was extracted.

From the nanowire dimensions given above, aspect ratios for both the silicon and rhodium nanowires are larger than 20 which justify the use of the 2D approximation in our theory and simulations. The forcing amplitude was controlled to keep the resonator displacement amplitude less than the gap height. The displacement amplitude was thus below 300 nm, corresponding to maximum velocities of 3.6 and 13.6 m/s for the rhodium and silicon nanoresonators, respectively. The mean molecular speed at T=295 K is 472.5 m/s, yielding maximum Mach numbers of 7.6×10^{-3} and 2.9×10^{-2} for the two resonators. This justifies the application of the BGK-LM-DSMC simulation technique to study these systems. Using resonant frequencies of 1.93 and 7.18 MHz for the silicon and rhodium nanowires, we find that the dimensionless number $\omega\tau_f \ll 1$ for the full range of Knudsen numbers thus justifying the use of the quasisteady simulation to explore this system. The dimensionless drag forces and Knudsen numbers shown in Fig. 7 have been calculated from the pressure and the Q-factor as outlined in Sec. I. This calculation requires that $Q^s=(2\pi E_{\text{stored}})/E^s_{\text{diss}}$, the part of the Q-factor associated with solid damping, be known. As explained in Sec. I, we obtain this from the low pressure asymptote in the experimental Q-factor versus pressure curve. For the silicon and rhodium nanowire resonators, the values were $Q^s=4580$ and $Q^s=1090$, respectively.

From Fig. 7, we see that, at very high Kn, unlike the case of the silicon nanowire, the experimental data for the Rhodium nanowire attains a constant value. This is because the rhodium nanowire, due to its intrinsic material properties, has higher solid damping compared to the silicon nanowire which in turn makes it less sensitive to the damping in the surrounding fluid at much higher pressures (lower Kn) than the silicon nanowire. However, at intermediate to high Kn, the drag force for both experimental systems approaches the scaling in the free molecular flow regime as predicted by both theory and simulations. Quantitatively, the experimentally measured drag force is nearly 25%–30% lower than that obtained from theory or simulations over the entire range of Kn explored. At small Kn, extrapolation appears to indicate that the experiments will yield a drag force that is smaller than that predicted by our slip theory or simulations (see inset in Fig. 7). The fact that the simulations agree with the slip theory and free molecular flow theory at small and large Kn, respectively, and that the slip theory approaches the continuum solution of Jeffery and Onishi suggests that there is no systematic error in the simulation results. The simulations assume that gas molecules undergo purely diffuse reflection from the solid surfaces corresponding to an accommodation coefficient for tangential momentum transport, α_t of 1. Experimental measurements indicate that $\alpha_t \approx 0.8$ for silicon surfaces.[35] At this value of α_t the drag on a sphere is reduced by less than 10% from its value at $\alpha_t=1$.[36] It therefore seems unlikely that imperfect momentum accommodation can account for the deviations between the experiment and theory and the reason for these deviations is unknown.

Based on our theoretical results for the scaling of the drag force with Kn in the continuum and free molecular flow regimes (Sec. III), we propose that the dimensionless drag force at any H/R be correlated with the form

$$\frac{F}{4\pi\mu U}=\frac{F^{(0)}}{4\pi\mu U}\left[\frac{1+A\text{Kn}}{1+B\text{Kn}+C\text{Kn}^2}\right], \tag{37}$$

where $F^{(0)}$, as defined earlier, is the drag force in the continuum limit and is given by Eq. (23) and A, B, and C are unknown coefficients that depend only on the distance between the nanowire and the wall and can be determined by the following procedure. For a given H/R, in the slip regime, using $\text{Kn}\to 0$ in Eq. (37) and comparing the result to the expression in the slip regime, Eq. (29), we obtain

$$A-B=\frac{F^{(1)}}{F^{(0)}}. \tag{38}$$

Similarly, in the free molecular flow regime, applying the limit $\text{Kn}\to\infty$ to Eq. (37) and comparing the resultant equation to the free molecular flow result, Eq. (36), we obtain

$$\frac{A}{C}=\frac{I_1}{8}\frac{4\pi\mu U}{F^{(0)}}. \tag{39}$$

A third relation between these coefficients is obtained by using Eq. (37) to evaluate the drag at an intermediate Knudsen number and equating to it to the drag force obtained at the same Knudsen via our quasisteady simulations. An intermediate value Kn=1 is used to generate the results reported in Table I for several values of H/R. The fit obtained using the asymptotic limits and the simulation data for Kn=1.0 gives good predictions for Kn=0.5 thus verifying our approach. The coefficients are well described by the curve fits given in the caption to Table I. With Eq. (37) and these curve fits, we thus have a semiempirical expression that can predict the dimensionless drag force at any Kn and for H/R in the range 0.5–4. In Fig. 8, we plot the nondimensionalized drag force obtained using our semiempirical expression as a func-

TABLE I. Coefficients A, B, and C in Eq. (37) as a function of H/R. The coefficients can be well-fitted by the following equations: $A=2.912\times\exp[-0.3351(H/R)]$, $B=3.7382(H/R)^{-0.5782}$, and $C=6.4283(H/R)^{-1.3704}$.

H/R	A	B	C
0.5	2.3445	5.092	14.9783
1.0	2.2194	4.0296	7.0203
1.8182	1.6694	2.9031	3.1957
2.0	1.3933	2.5529	2.4836
4.0	0.7619	1.524	0.8673

tion of Kn at different H/R. For comparison, we again plot our simulation results obtained at $H/R=1.8182$ from which we find that our expression describes the simulation data very well.

B. Unsteady regime ($\omega\tau_f \gg 1$)

In Fig. 9, we plot the nondimensionalized fluid drag coefficient $\zeta_R/(4\pi\mu)$ as a function of the normalized oscillation frequency $\omega\tau$ for different Kn, where τ is the BGK relaxation time defined in Sec. II. As per the definition given in Sec. I, for quasisteady flows, this nondimensionalized drag coefficient will reduce to the nondimensional drag force $F/(4\pi\mu U)$ presented earlier. From the figure, we see that, for high Kn, the drag coefficient exhibits a very small decrease with increasing $\omega\tau$. For low Kn, the drag coefficient has plateaus for both low ($\omega\tau<1$) and high ($\omega\tau>1$) frequencies and increases with frequency in the intermediate regime of $\omega\tau\sim 1$. The low frequency drag is in good agreement with results from our quasisteady simulations. For $\mathrm{Kn}=O(1)$, the transition between low frequency and high frequency behavior is expected to occur at $\omega\tau=O(1)$ which appears to be consistent with our Kn=2.0 and Kn=4.0 simulation data. In the near-continuum regime, $\mathrm{Kn}\ll 1$, the transition begins when $\omega R^2/\nu\sim\omega\tau/\mathrm{Kn}^2\sim O(1)$ when the quasicontinuum flow becomes unsteady. As the frequency is increased the quasicontinuum flow develops a boundary layer of thickness $(\nu/\omega)^{1/2}$ which becomes comparable with the mean free path λ when $\mathrm{Kn}\sim O(1)$. Thus, the transition extends over the range $O(1)\leq\omega\tau\leq O(\mathrm{Kn}^2)$. Our simulations confirm the existence of such a wide transition regime at low Knudsen numbers. Moreover, this transition appears to begin at a slightly lower frequency for Kn=0.1 when compared to Kn=0.2 which is consistent with the $O(\mathrm{Kn}^2)$ scaling predicted for the lower frequency limit at which the transition is expected to begin for $\mathrm{Kn}\ll 1$. This trend does not carry over to Kn=0.5 data possibly because this Knudsen number can no longer be treated as being much smaller than 1. Figure 10 shows a plot of the constant drag coefficient obtained at low and high frequencies as a function of Kn. It is interesting to note that the high frequency asymptotes exhibit a 1/Kn scaling and are in good quantitative agreement with the theoretical free molecular flow result for an isolated cylinder in the quasisteady regime [Eq. (36) with $I_1=0.5(6+\pi)$] even at

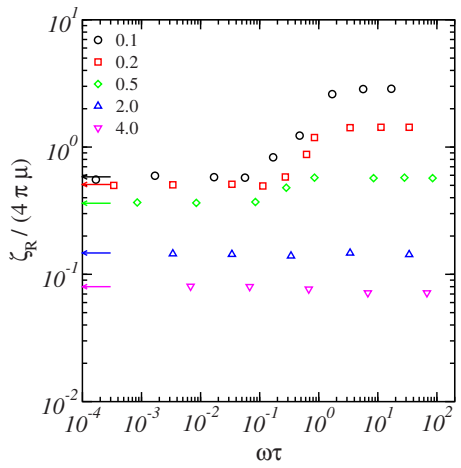

FIG. 9. (Color online) Simulation results for the normalized drag coefficient as a function of nondimensionalized oscillation frequency $\omega\tau$ at different Kn where $\tau=(4/\pi)(\lambda/\langle c\rangle)$ is the BGK relaxation time defined in Sec. II. The arrows near the y-axis represent quasisteady simulation results. Error bars in simulations are smaller than symbol size.

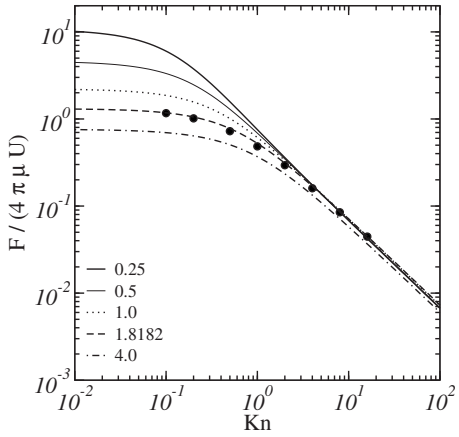

FIG. 8. Normalized drag force per unit length as a function of Kn for different H/R as given in the legend. Lines represent predictions obtained using the semiempirical expression given in Eq. (37) and curve fits for coefficients in that equation. Symbols represent simulation data at $H/R=1.8182$. Error bars in simulations are smaller than symbol size.

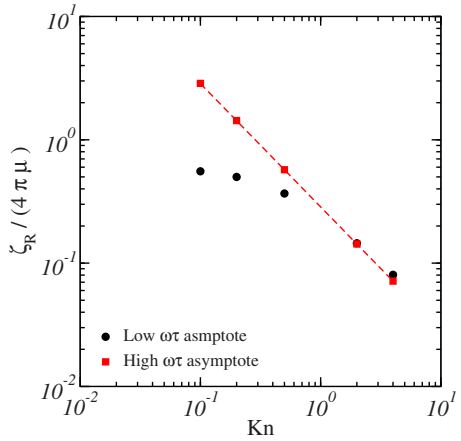

FIG. 10. (Color online) Low and high frequency asymptotes for the normalized drag coefficient plotted as a function of Kn. Symbols represent simulation data and the dashed line represents the drag coefficient for an isolated nanowire in the free molecular flow regime. This free molecular flow result is given by Eq. (36) with $I_1=0.5(6+\pi)$ (Ref. 34). Error bars in simulations are smaller than symbol size.

small Knudsen numbers. This is consistent with the finding of Park *et al.*[21] that the drag in planar Couette flow at high frequencies is the same as the quasisteady drag at high Knudsen numbers. At high frequencies, $\omega\tau \gg 1$ implies that by the time a molecule reflected from the solid surface can undergo an intermolecular collision and return to the nanowire, the nanowire would have had many periods of oscillation and the return trip will come at a phase of the wire oscillation that is uncorrelated with the phase at which the original molecule-nanowire collision occurred. Thus the nanowire just sees a reservoir of equilibrium Maxwellian molecules and the system effectively behaves as if an isolated nanowire is oscillating under free molecular flow conditions. One important consequence of this effect that we see in Fig. 10 is that at high Kn ($\mathrm{Kn} \geq 2.0$) the high frequency drag is somewhat lower than the low frequency drag. At high Kn and low frequencies, the drag force is given by the free molecular flow result for a nanowire near a wall whereas at high Kn and high frequencies, because of the aforementioned effect, the drag force is given by the free molecular flow result for an isolated cylinder which is slightly smaller.

A final comment needs to be made about how the theory and simulations compare to experimental data obtained by Karabacak and co-workers.[14,37] The experimental data, when reduced to the same nondimensional format shown in Fig. 9, did not show good agreement with theory/simulations even on a qualitative level. This lack of agreement is a result of large statistical scatter in the experimental data coupled with the fact that, in their experiments, the authors simultaneously vary more than one parameter. For example, at any given ambient gas pressure, they vary the resonance frequency by changing the width and thickness of the nanowire which leads to variations in the Knudsen number as well. It should be noted that, in their article, the authors compared their experiments to Ref. 19's theoretical predictions for the friction factor for tangential oscillation of a planar wall as a function of resonance frequency at a given ambient pressure and reported good agreement (within statistical error) provided the theoretical results were scaled up by an arbitrary geometrical correction factor of 2.8. However, such a comparison is not correct. For fixed nanowire dimensions, changing ambient gas pressure changes the mean free path and the noncontinuum nature of flow thereby affecting the drag force. Thus, data comparisons should strictly be performed at a fixed Knudsen number rather than a fixed pressure. This condition is clearly violated in the comparisons shown in Ref. 14 where, at a given pressure, the nanowire dimensions change with resonance frequency thereby affecting the Knudsen number.

V. CONCLUSIONS

It is clear that resonating nanowires offer several advantages over their micro-/macrocounterparts in sensitivity of measurement as well as energy requirement, especially at lower pressures. This is due to the comparable values for the mean free path of the gas and nanowire dimensions which lead to extremely low dissipation and high Q-factors. Recent experiments have attempted to characterize these devices in terms of Q-factors as a function of pressure (or Knudsen number). These studies, although qualitatively similar in their findings, disagree with each other significantly. In this article, we have used theory and simulations to provide a framework in which to understand existing experimental data and design further tests for providing sufficient information with which to characterize drag.

Both the theory and simulations assume that the nanowires have large enough aspect ratios so that the problem can be treated as two-dimensional. They also apply a small Mach number approximation which is valid only for nanowires moving at speeds smaller than the thermal speed of the gas molecules. It should be noted, however, that this restriction is necessary in order to justify the linear treatment of the amplitude of the resonator leading to the definition of a quality factor. The theory is valid only for the quasisteady regime where the characteristic fluid relaxation time is much smaller than the nanowire oscillation time period. The simulations treat both the quasisteady and the unsteady regimes. We have studied the variation in the normalized drag force exerted by the fluid on the oscillating nanowire as a function of Knudsen number.

In the quasisteady regime, our simulation results are in excellent agreement with asymptotic theories for both the high and low Knudsen regimes and appear to be approaching the Jeffrey–Onishi continuum predictions as $\mathrm{Kn} \to 0$. We also compare our theory/simulations with Li *et al.*'s[7] experimental data on silicon and rhodium nanowires, which, as discussed in Sec. IV A, satisfies all of the assumptions inherent in our theory and simulations. Our comparison indicates that, over the entire range of Kn studied, experiments yield drag forces that are nearly 20%–30% lower than theoretical predictions. Using our simulation and theoretical results, we have developed a semiempirical expression that can be used to calculate the drag force for any given Kn and distance between the nanowire and the bottom substrate.

As seen in Sec. I, some of the experimental literature also spans the unsteady regime, $\omega\tau_f = O(1)$ and consequently we also performed simulations to understand the effect of unsteady flows on the drag force. These simulations indicate that, while at high Kn, the drag force is nearly invariant with frequency, at low Kn, the drag force exhibits three different scaling regimes, a low frequency and a high frequency regime, where the drag force is independent of frequency, and an intermediate regime where the drag force increases with frequency so as to bridge the low frequency and high frequency asymptotes. As the Knudsen number decreases, the range of frequencies over which the drag coefficient varies increases reflecting the development of a viscous boundary layer near the wire surface. Our efforts to perform a thorough comparison between our simulations and unsteady experimental data obtained by Karabacak and co-workers[14] were thwarted because of the fact that changes in the oscillation frequency in these experiments also caused other experimental parameters to change. More controlled experiments are needed to verify these theories/simulations.

ACKNOWLEDGMENTS

This work was supported by NSF Grant No. CBET-0730579.

[1]C. Gui, R. Legtenberg, H. Tilmans, J. Fluitman, and M. Elwenspoek, "Nonlinearity and hysteresis of resonant strain gauges," J. Microelectromech. Syst. **7**, 122 (1998).
[2]M. Zalalutdinov, A. Olkhovets, A. Zehnder, B. Ilic, D. Czaplewski, H. G. Craighead, and J. M. Parpia, "Optically pumped parametric amplification for micromechanical oscillators," Appl. Phys. Lett. **78**, 3142 (2001).
[3]J. D. Zook, D. W. Burns, H. Guckel, J. J. Sniegowski, R. L. Engelstad, and Z. Feng, "Characteristics of polysilicon resonant microbeams," Sens. Actuators, A **35**, 51 (1992).
[4]R. B. Bhiladvala and Z. J. Wang, "Effect of fluids on the Q factor and resonance frequency of oscillating micrometer and nanometer scale beams," Phys. Rev. E **69**, 036307 (2004).
[5]K. L. Ekinci and M. L. Roukes, "Nanoelectromechanical systems," Rev. Sci. Instrum. **76**, 061101 (2005).
[6]M. Li, H. L. Tang, and M. L. Roukes, "Ultra-sensitive NEMS-based cantilevers for sensing, scanned probe and very high-frequency applications," Nat. Nanotechnol. **2**, 114 (2007).
[7]M. Li, R. B. Bhiladvala, T. J. Morrow, J. A. Sioss, K. Lew, J. M. Redwing, C. D. Keating, and T. S. Mayer, "Bottom-up assembly of large-area nanowire resonator arrays," Nat. Nanotechnol. **3**, 88 (2008).
[8]L. Sekaric, M. Zalalutdinov, R. B. Bhiladvala, A. T. Zehnder, J. M. Parpia, and H. G. Craighead, "Operation of nanomechanical resonant structures in air," Appl. Phys. Lett. **81**, 2641 (2002).
[9]K. Yum, Z. Wang, A. P. Suryavanshi, and M. Yu, "Experimental measurement and model analysis of damping effect in nanoscale mechanical beam resonators in air," J. Appl. Phys. **96**, 3933 (2004).
[10]F. M. Battiston, J. P. Ramseyer, H. P. Lang, M. K. Baller, C. Gerber, J. K. Gimzewski, E. Meyer, and H. Güntherodt, "A chemical sensor based on a microfabricated cantilever array with simultaneous resonance-frequency and bending readout," Sens. Actuators B **77**, 122 (2001).
[11]W. Liu, V. Montana, E. R. Chapman, U. Mohideen, and V. Parpura, "Botulinum toxin type B micromechanosensor," Proc. Natl. Acad. Sci. U.S.A. **100**, 13621 (2003).
[12]B. Ilic, D. Czaplewski, M. Zalalutdinov, H. G. Craighead, P. Neuzil, C. Campagnolo, and C. Batt, "Single cell detection with micromechanical oscillators," J. Vac. Sci. Technol. B **19**, 2825 (2001).
[13]P. Poncharal, Z. L. Wang, D. Ugarte, and W. A. de Heer, "Electrostatic deflections and electromechanical resonances of carbon nanotubes," Science **283**, 1513 (1999).
[14]D. M. Karabacak, V. Yakhot, and K. L. Ekinci, "High-frequency nanofluidics: An experimental study using nanomechanical resonators," Phys. Rev. Lett. **98**, 254505 (2007).
[15]K. Y. Yasumura, T. D. Stowe, E. M. Chow, T. Pfafman, T. W. Kenny, B. C. Stipe, and D. Rugar, "Quality factors in micron- and submicron-thick cantilevers," J. Microelectromech. Syst. **9**, 117 (2000).
[16]D. J. Jeffrey and Y. Onishi, "The slow motion of a cylinder next to a plane wall," Q. J. Mech. Appl. Math. **34**, 129 (1981).
[17]R. J. Clarke, S. M. Cox, P. M. Williams, and O. E. Jensen, "The drag on a microcantilever oscillating near a wall," J. Fluid Mech. **545**, 397 (2005).
[18]K. Yamamoto and K. Sera, "Flow of a rarefied gas past a circular cylinder," Phys. Fluids **28**, 1286 (1985).
[19]V. Yakhot and C. Colosqui, "Stokes' second flow problem in a high-frequency limit: Application to nanomechanical resonators," J. Fluid Mech. **586**, 249 (2007).
[20]F. Sharipov and D. Kalempa, "Gas flow near a plate oscillating longitudinally with an arbitrary frequency," Phys. Fluids **19**, 017110 (2007).
[21]J. H. Park, P. Bahukudumbi, and A. Beskok, "Rarefaction effects on shear driven oscillatory gas flows: A direct simulation Monte Carlo study in the entire Knudsen regime," Phys. Fluids **16**, 317 (2004).
[22]N. G. Hadjiconstantinou, "Oscillatory shear-driven gas flows in the transition and free-molecular-flow regimes," Phys. Fluids **17**, 100611 (2005).
[23]S. Ramanathan and D. L. Koch, "An efficient direct simulation Monte Carlo method for low Mach number noncontinuum gas flows based on the Bhatnagar–Gross–Krook model," Phys. Fluids **21**, 033103 (2009).
[24]G. A. Bird, *Molecular Gas Dynamics and the Direct Simulation of Gas Flows* (Oxford University Press, New York, 1994).
[25]P. L. Bhatnagar, E. P. Gross, and M. Krook, "A model for collision processes in gases. I. Small amplitude processes in charged and neutral one-component systems," Phys. Rev. **94**, 511 (1954).
[26]N. G. Hadjiconstantinou and A. L. Garcia, "Statistical error in particle simulations of low Mach number flows," *First MIT Conference on Computational Fluid and Solid Mechanics*, Cambridge, MA, 12–14 June 2000 (Elsevier Science, Oxford, 2001).
[27]M. A. Rieffel, "A method for estimating the computational requirements of DSMC simulations," J. Comput. Phys. **149**, 95 (1999).
[28]A. Gopinath and D. L. Koch, "Hydrodynamic interactions between two equal spheres in a highly rarefied gas," Phys. Fluids **11**, 2772 (1999).
[29]G. K. Batchelor, *An Introduction to Fluid Dynamics* (Cambridge University Press, New York, 2000).
[30]C. Cercignani and D. H. Sattinger, *Scaling Limits and Models in Physical Processes* (Birkhauser, Basel, Switzerland, 1998).
[31]N. G. Hadjiconstantinou, "Comment on Cercignani's second-order slip coefficient," Phys. Fluids **15**, 2352 (2003).
[32]R. Sundararajakumar and D. L. Koch, "Non-continuum lubrication flows between particles colliding in a gas," J. Fluid Mech. **313**, 283 (1996).
[33]C. Cercignani, *The Boltzmann Equation and Its Applications* (Springer-Verlag, New York, NY, 1988).
[34]A. Gopinath and D. L. Koch, "A method for calculating hydrodynamic interactions between two bodies in low Mach number free-molecular flows with application to the resistivity functions for two aligned cylinders," Phys. Fluids **9**, 3550 (1997).
[35]E. B. Arkilic, K. S. Breuer, and M. A. Schmidt, "Mass flow and tangential momentum accommodation in silicon micromachined channels," J. Fluid Mech. **437**, 29 (2001).
[36]S. A. Beresnev, V. G. Chernyak, and G. A. Fomyagin, "Motion of a spherical particle in a rarefied gas. Part 2. Drag and thermal polarization," J. Fluid Mech. **219**, 405 (1990).
[37]D. M. Karabacak, "Resonant operation of nanoelectromechanical systems in fluidic environments," Ph.D. thesis, Department of Aerospace and Mechanical Engineering, Boston University, Boston, MA, 2008.